Published in final edited form as:
J Phys Chem B. 2013 April 25; 117(16): 4604–4610. doi:10.1021/jp3087978.

Tuning Nanostructure Dimensions with Supramolecular Twisting

Tyson J. Moyer[a], **Honggang Cui**[a,b], and **Samuel I. Stupp**[a,c,d,e]
[a]Department of Materials Science, Northwestern University

[c]Department of Chemistry, Northwestern University

[d]Department of Medicine, Northwestern University

[e]Institute for BioNanotechnology in Medicine (IBNAM), Northwestern University

Abstract

Peptide amphiphiles are molecules containing a peptide segment covalently bonded to a hydrophobic tail and are known to self-assemble in water into supramolecular nanostructures with shape diversity ranging from spheres to cylinders, twisted ribbons, belts, and tubes. Understanding the self-assembly mechanisms to control dimensions and shapes of the nanostructures remains a grand challenge. We report here on a systematic study of peptide amphiphiles containing valine-glutamic acid dimeric repeats known to promote self-assembly into belt-like flat assemblies. We find that lateral growth of the assemblies can be controlled in the range of 100 nm down to 10 nm as the number of dimeric repeats is increased from two to six. Using circular dichroism, the degree of β-sheet twisting within the supramolecular assemblies was found to be directly proportional to the number of dimeric repeats in the PA molecule. Interestingly, as twisting increased a threshold is reached where cylinders rather than flat assemblies become the dominant morphology. We also show that in the belt regime, the width of the nanostructures can be decreased by raising the pH to increase charge density and therefore electrostatic repulsion among glutamic acid residues. The control of size and shape of these nanostructures should affect their functions in biological signaling and drug delivery.

Keywords

Chiral self-assembly; peptide amphiphiles; cryo-TEM; twisted ribbons

Introduction

Learning to tune the size and shape of supramolecular structures in solution has been an important goal in chemistry motivated by the search for novel functional systems and a better understanding of biological self-assembly. Using non-covalent interactions between small molecule subunits, supramolecular polymers have a wide range of potential applications in both biology and electronics.[1] The self-assembly of these molecules can produce a vast array of nanostructures after undergoing directional polymerization;[2,3] however, these morphologies are often difficult to control in multiple dimensions. The monomer subunits that undergo self-assembly span a large size range from proteins, including microtubules[4] and amyloids[5], to small molecules, such as carbohydrates[6] and

Correspondence to: Samuel I. Stupp.

[b]Present address: Department of Chemical Engineering, Johns Hopkins University, Baltimore MD

Supporting Information: Supporting information contains molecular and nanostructure characterization, including mass spectrometry, cryo-TEM, and SAXS. This information is available free of charge via the Internet at http://pubs.acs.org.

oligopeptides.[7] Specifically for small molecule assemblies, chirality has a significant impact on the one-dimensional growth of nanostructures,[8,9] and can determine shape[10,11] and gelation[12] properties. For biological applications, tuning the size and shape of these assembled nanostructures is an important consideration in terms of materials design, especially in the delivery of chemotherapeutic agents. The effect of size has been demonstrated by the tumor-targeting abilities of nanoscale particles through the enhanced permeability and retention (EPR) effect.[13] In addition to size, shape plays an important role in effective delivery; previous reports have shown shape-dependent behavior of nanostructures *in vitro*[14] and *in vivo*.[15] These studies suggest that the ability to tune the size and shape of nanostructures is an essential parameter for biological applications.

Numerous cases of tunable supramolecular polymers occur in nature. One type of such morphological control involves the use of twisting to constrain growth in one dimension. In the radial growth of filaments composed of the blood-clotting protein fibrin, the radius is found to be limited by twisting because a higher pitch imparts a strain at the outer edges of the fiber.[16] Additionally, the proteins lysozyme and β-lactoglobulin are able to form amyloid nanoribbons upon heating that have widths proportional to the pitch.[17] Under different self-assembly conditions, β-lactoglobulin can also form cylindrical amyloid fibrils with a superhelical pitch that is proportional to fiber diameter,[18] as well as the electrostatic repulsion.[19] It is also known that in DNA assemblies the number of base pairs per turn can be used to control their degree and direction of twisting.[20] For amyloid assemblies, chirality-induced twisting within fibers has been reported to limit the size of self-assembled structures. [21,22] Additionally, the helical pitch of ribbon-like, amyloid structures formed from short peptides has been altered by the addition of hydrophobic residues.[23] Within peptide-based structures, hydrogen bonded β-sheets have a natural twist resulting from the inherent chirality of the molecules.[24,25] Sequences containing β-sheet forming residues, such as polyalanine, have shown twisting by circular dichroism (CD).[26] This type of hydrogen bonding has been demonstrated to lead to formation of both ribbons and cylinders for self-assembling peptides.[24] Time-dependent studies of peptide assemblies have shown transitions in morphology over time from twisted ribbons to helical ribbons to cylindrical tubes, demonstrating the importance of chirality-induced twisting on dynamic assemblies.[27]

Self-assembling peptide sequences conjugated to a hydrophobic alkyl tail have been developed by our group that are known to self-assemble into one-dimensional nanostructures.[28,29] In these peptide amphiphiles (PAs), at least part of the peptide sequence forms β-sheets and the alkyl tail leads to their hydrophobic collapse in water to create the core of the nanostructure. The combination of these elements produces high-aspect-ratio, 1-D structures with high persistence lengths. Functional peptide sequences can be conjugated at one terminus of the peptide for display on the surfaces of the nanofibers, for example to present specific signals to cells.[30] PAs have been used in a variety of applications, including angiogenesis within ischemic tissue,[31] bone regeneration,[32] central nervous system repair,[33] and tumor growth inhibition.[34,35] Twisted assemblies of PAs have been reported previously,[36] and have also been shown to have an effect on PA gel stiffness.[37] Using CD and Fourier transform infrared (FTIR) spectroscopy, these reports quantified the level of twisting within cylindrical peptide amphiphile assemblies. In addition to cylindrical morphologies, previous work has shown that an alternating sequence of a hydrophobic (V) and a charged amino acid (E) in PAs leads to large belt-like supramolecular assemblies without any curvature.[38] This specific PA, C_{16}-VEVE, produced structures with dimensions of over 100 nm in width, 5 nm in thickness, and several microns in length. Belt-like structures[39] and helical ribbons[40] have been observed in other lipidated peptides as well. Inspired by these previous studies we have investigated here the supramolecular structure of a series of PAs containing VE dimer sequences of various lengths. The objective has been to identify molecular factors playing a role in the tuning of shape and dimensions of these

nanostructures. The work has involved the use of cryogenic electron microscopy, small-angle x-ray scattering, atomic force microscopy, and circular dichroism to characterize the assembly behavior of (VE) dimer PAs in aqueous solutions.

Materials and Methods

PA synthesis

PAs were synthesized using standard Fmoc solid-phase synthesis protocols. Coupling reactions were performed using Fmoc-amino acids (4 equiv), O-benzotriazole-*N,N,N′,N′*-tetramethyluronium-hexafluorophosphate (HBTU) (3.95 equiv) and N,N-diispropylethylamine (DIEA) (6 equiv) in N,N-dimethylformamide (DMF). The alkyl tail of the PAs was added by reacting the N-terminus with palmitic acid (4 equiv), HBTU (3.95 equiv) and DIEA (6 equiv) in DMF. Following cleavage using a TFA/triisopropylsilane (TIPS)/H_2O mixture (95:2.5:2.5), PAs were purified by high-performance liquid chromatography (HPLC) on a Varian Prostar 210 HPLC system, eluting with 2% acetonitrile (MeCN) to 100% MeCN in water on a Phenomenex C18 Gemini NX column (150 × 30 mm) with 5 μm pore size and 110 Å particle size. Product-containing fractions were confirmed by electrospray ionization (ESI) mass spectrometry (Agilent 6510 Q-TOF LC/MS), combined, and lyophilized after removing MeCN by rotary evaporation. ESI was performed on all purified products (Figure S1).

TEM characterization

Cryogenic TEM (cryo-TEM) specimens were prepared using an FEI Vitrobot. A 5 μL drop of a 5 mM PA solution at pH 7, unless specified otherwise, was pipetted onto a lacey carbon grid at room temperature. Samples were blotted in 95% humidity, subsequently plunged into liquid ethane, and stored in liquid N_2 prior to imaging. Images were taken using a JEOL 1230 transmission electron microscope operating at 100 keV equipped with a Gatan camera. All values of widths were the average of at least 75 measurements.

SAXS studies

Small angle X-ray scattering (SAXS) experiments were performed at the Advanced Photon Source, Argonne National Laboratory. The X-ray energy (15 keV) was selected using a double-crystal monochromator, and the SAXS CCD camera was offset in order to achieve a wide range of scattering angles. Samples were dissolved at a concentration of 5 mM and placed in 1.5 mm quartz capillary tubes. The typical incident X-ray flux on the sample was ~1×10^{12} photons/s with a 0.2×0.3 mm^2 collimator, estimated by a He ion channel, and samples were irradiated for 5 s. The 1D scattering profiles were obtained by azimuthal integration of the 2D patterns, with scattering from the capillaries subtracted as background. Scattering profiles were then plotted on a relative scale as a function of the scattering vector $q = (4\pi/\lambda)\sin(\theta/2)$, where θ is the scattering angle. Fits of the scattering curves were performed using a core-shell parallelpiped model, as outlined in the supplemental information.[41]

AFM

Atomic force microscopy (AFM) was performed using dried samples to characterize height and structure morphology. At a concentration of 1 mM, PA samples were drop cast on silicon and dried in preparation for AFM. Measurements were taken on a MultiMode Scanning Probe Microscope using a silicon nitride tip.

Circular Dichroism

Circular dichroism (CD) was performed on a circular dichroism spectrophotometer J-815. For sample preparation, 30 μL of 10 mM samples of PA were gelled with 3 μL of 0.2 M CaCl2 and aged for 15 minutes. The gels were diluted with 1 mL of water and vortexed vigorously until the sample was completely dissolved, yielding a final PA concentration of 0.3 mM. Data represents an average of three accumulations, taken at 50 nm/min with a data pitch of 0.2 nm. For pH dependent studies, the pH of the initial 10 mM solutions as well as the diluted samples were adjusted with 0.2 M NaOH to specified values.

Results and Discussion

Cryo-TEM of $(VE)_x$ Molecules

In order to determine the effect of additional amino acids on dimensions and supramolecular structures of these peptide amphiphiles, cryo-TEM was performed on each of the $(VE)_x$ molecules. Confirming previous reports, the $(VE)_2$ molecule formed large, flat nanobelts that are 100s of nanometers in width (Figure 1B). The images also show narrower belts with darker contrast, which are simply nanobelts tilted from the plane of view. After two weeks in solution, the nanobelt morphology did not show any increase in twisting or change in morphology (Figure S2). In comparison to $(VE)_2$, $(VE)_4$ exhibits less lateral growth by cryo-TEM, forming ribbon-like structures that are roughly 40 nm in width (Figure 1C). Other than width, an important difference to note between the $(VE)_2$ and $(VE)_4$ structures is the pitch, which we define as the distance between twists observed in the nanostructures (Figure S3A). $(VE)_2$ displays occasional twists that are spaced on average 2.3 ± 1.1 μm apart. We observed smaller pitches of 0.81 ± 0.49 μm for $(VE)_4$, suggesting a relationship between pitch and width (Figure S3B). As previously described, amyloid assemblies of lysozyme demonstrate that the pitch measured by TEM is directly related to the twisting in nanostructures.[17] While the observed pitches were polydisperse in length, the positive correlation suggested that pitch determined the width of the nanostructure. In the case of $(VE)_4$, an increase in the degree of twisting appears to result in less lateral growth of the flat nanostructure. Previous studies have in the case of amyloid fibrils, the incorporation of twisted ribbons into fibrils was limited due to an elastic distortion penalty.[24] In the case of the dimeric PAs, we believe that an analogous situation occurs, where the twist in supramolecular structure imposes an elastic penalty that limits lateral growth. Overall, while both $(VE)_2$ and $(VE)_4$ formed flat structures in solution, $(VE)_2$ assembled into much wider structures that appeared to be less twisted by cryo-TEM.

The addition of more VE units had an even greater effect on morphology in solution. By cryo-TEM, $(VE)_6$ appears to form a mixture of cylinders and narrow ribbons, demonstrating a shift from flat to cylindrical structures in solution (Figure 1D). A common feature of the flat structures of $(VE)_6$ was splitting into two distinct cylindrical structures (Figure S4). While splitting of the ribbon structure was observed frequently for $(VE)_6$ nanostructures, this effect was not seen in the assemblies of $(VE)_2$ and $(VE)_4$. The $(VE)_6$ nanostructure splitting suggested that the ribbon structure was composed of individual cylindrical components that can aggregate into larger, flat morphologies. The coexistence of small, flat structures along with cylinders demonstrated that $(VE)_6$ was at a transition point between flat and curved supramolecular structures. This molecule appeared to assemble into structures that generally had both uniform width and contrast (Figure S5). Unfortunately, the resolution by cryo-TEM was not high enough to determine if these observed one-dimensional structures are cylinders or highly twisted ribbons. However, because the majority of structures had uniform contrast and no visible twist, these images suggest the existence of cylindrical structures in solution for $(VE)_6$, and that $(VE)_6$ is close to the transition point between ribbons and cylinders.

Small-Angle X-Ray Scattering

In order to confirm the results from cryo-TEM, small-angle x-ray scattering (SAXS) was performed on each of the molecules in solution. SAXS is a technique used to determine the size and shape of nanostructures in solution.[42] For $(VE)_2$, the SAXS results confirmed previously published small-angle neutron scattering (SANS) on the same molecule that showed a −2 slope in the low-q region, demonstrating the presence of flat structures in solution.[38] A Bragg peak was observed at a lower pH ~6.5 for $(VE)_2$, which suggested the stacking of multiple nanobelt structures in solution (Figure S6). This Bragg peak corresponded to a d-spacing of 3.9 nm, which was shorter than the expected height of two stacked molecules (6.6 nm), suggesting interdigitation of the alkyl tails. However, this peak was no longer visible after adjusting the pH to 7.0, demonstrating that as the carboxylic acid groups are deprotonated to carboxylate groups, stacking of multiple belt structures was no longer favorable (Figure 2A). In the low-q regime, the gradual change in slope for $(VE)_2$, $(VE)_4$, and $(VE)_6$ showed a shift from −2 to −1.5, which suggested a change from a flat shape to structures with more finite lateral dimensions. An additional explanation for the change in slope could be a heterogeneous mixture of both flat (−2 slope) and cylindrical structures (−1 slope) in solution for the case of $(VE)_6$. A −4 slope in the high-q region for all of the peptides indicated a sharp interface between the solvent and structures.

To obtain more information about the dimensions and shape of the molecules in solution, a core-shell parallelepiped fit was applied to each scattering curve. This model included a rectangular core, with shell thicknesses in both the x and y dimensions, while the z (longest) dimension contained no shell (Figure S7). The scattering curves of nanostructures formed by $(VE)_2$, $(VE)_4$, and $(VE)_6$ PAs were all fit with this model and constraints. In the case of $(VE)_2$, the dimensions were found to be 140 nm in width and 5 nm in thickness. While the width from this model was significantly larger than the one determined by cryo-TEM, this difference could be the result of some belt structures not being perfectly perpendicular to the direction beam, causing them to appear smaller than their actual width. This same model was then used to fit the $(VE)_4$ case, yielding a width of 22 nm and thickness of 4 nm. For $(VE)_6$, a fit using 13 nm in width and 8 nm in thickness indicated a much thinner structure. The variation in fit at the high-q range was likely the result of polydispersity in the sample, which was not accounted for in this model. One possible explanation for the differences observed by the SAXS fit and cryo-TEM was that the rectangular structure indicated by SAXS was actually the aggregation of two cylinders. The dimensions of these parallelepipeds for the different structures showed the same general trend seen by cryo-TEM (Figure 2b). These results confirmed the observations made by cryo-TEM of the transition from structures with widths on the order of 100 nm to significantly thinner morphologies with dimensions between 10 and 20 nm by increasing the number of amino acids on the PA. These scattering patterns demonstrated the presence of flat nanostructures in solution, and showed a general decrease in the width of the nanostructures as the number of amino acids increased.

Atomic Force Microscopy

Atomic force microscopy (AFM) was used to investigate the transition from flat to cylindrical nanostructures. Long, flat structures were observed for both $(VE)_2$ and $(VE)_4$ (Figure 3A,B). Confirming the results from cryo-TEM, $(VE)_2$ has significantly larger widths compared to $(VE)_4$. Comparisons of the z-heights show a mesa-like shape for both $(VE)_2$ and $(VE)_4$ (Figure S8A,B). The majority of the heights of the observed structures were larger than the expected values for a single bilayer; this increase was likely the result of stacking of multiple nanostructures. In the case of $(VE)_4$, grooves were evident in the single bilayer structures (Figure 3B). These grooved structures have been observed previously for $(VE)_2$ after the addition of NaOH, as observed by conventional TEM.[38] Fraying was also

observed near the end of the $(VE)_4$ nanostructures. While it could be a sample-preparation effect, the fraying suggested that the flat structures for $(VE)_4$ are composed of individual cylinders that begin to delaminate near the ends. A similar effect was observed previously for $(VE)_2$ by conventional TEM, although this structure frayed into much smaller ribbon morphologies.[38] This observed fraying in $(VE)_4$ also suggests that the forces that hold the nanostructures together in the longitudinal direction, likely hydrogen bonding, are stronger than forces in the transverse direction. This fraying is comparable to the splitting observed for $(VE)_6$ nanostructures by cryo-TEM; however, an important distinction is that the observed fraying for $(VE)_6$ is composed of multiple cylindrical components, instead of just two as observed by cryo-TEM. These results suggest that the assembly method is the same for each of these molecules, and that the number of cylindrical structures that can stack together in lamellar form is limited by the number of (VE) residues. For $(VE)_6$, a mix of cylindrical and more aggregated flat structures was observed (Figure 3C). Analysis of the z-height shows that the majority of structures have a curved surface, in contrast to the flat structures observed for $(VE)_2$ and $(VE)_4$ (Figure S8C). The bending rigidity of $(VE)_6$ also appears lower when compared to the flat structures of $(VE)_2$ and $(VE)_4$. We expect that the energy to bend a cylinder about its axis is lower than that required to bend a ribbon about its long axis, which typically lies parallel to the surface when dried for AFM. Bending about the long axis is expected to be difficult because of the necessary molecular strain to produce this supramolecular deformation in the ribbon. We observed that the bending of ribbons occurs readily about the short axis when the structure folds across itself (Figure 3A); however, we did not observe deformation of ribbons along their long axis. These differences in structure determined by AFM were again consistent with the results from cryo-TEM. Overall, AFM demonstrates a transition from flat structures for $(VE)_2$ and $(VE)_4$ to cylindrical structures for $(VE)_6$.

Circular Dichroism

We used CD to characterize the secondary structure of these supramolecular polymers, and determine the relationship between intermolecular packing and nanostructure twisting. Previous reports have shown that a red-shift in the minimum around 215 nm in the CD curve corresponds to increased twisting or disorder in the β-sheet hydrogen bonds for PAs.[36,43] Additionally, previous studies have attributed red-shifted β-sheet CD curves to an increase in twisting. [26,44] In Figure 4a, the CD pattern of the $(VE)_x$ series was plotted. The degree of red-shifting appeared to increase with the addition of (VE) units, which suggested that a larger number of (VE) dimers induce twisting in β-sheets. These results confirmed previous theoretical studies that increasing the number of valines produced a red-shift in the CD spectrum. The amount of red-shift for each PA investigated was then quantified and plotted versus the observed widths to demonstrate their correlation to β-sheet twisting (Figure 4B). The degree of twisting in β-sheets appeared to limit the lateral growth of these nanostructures. The proposed structures based on this twisting are drawn in figure 4C–E. In $(VE)_2$, the lowest degree of β-sheet twisting along the long axis resulted in the most lateral growth (Figure 4C). We proposed that as the number of amino acids able to participate in hydrogen bonding increased, the lateral growth became constrained (Figure 4D). Eventually the observed structures were twisted to the point where they appear cylindrical (Figure 4E). Our results here results indicate that the side-chain interactions among β-sheets were affected by twisting, which was correlated with nanostructure width.

pH Dependence

In addition to the twist of supramolecular structures after β-sheet formation, we also expect the electrostatic repulsion among glutamic acid residues to play a role in limiting lateral growth. The twisting observed by CD could be attributed to the β-sheet forming valine residue or the negatively charged glutamic acids. To determine the role of electrostatic

repulsion, we examined the change in structure of $(VE)_2$ after incrementally increasing pH by the addition of NaOH. At higher pH, the number of deprotonated glutamic acid residues was expected to increase, increasing the repulsion among molecules. This repulsion would then limit lateral growth $(VE)_2$, and result in the smaller supramolecular structures observed by cryo-TEM (Figure 5A,B,C). At pH 8, a ribbon-like morphology is observed, with an average width of 45 nm. Additionally, the size distribution at pH 8 increased relative to pH 7 and pH 9, due to the presence of both larger (~70 nm) and smaller (~30 nm) flat structures in solution (Figure 4D). The $(VE)_2$ molecule at pH 8 now adopts a morphology more closely resembling the structure of $(VE)_4$ at pH 7 rather than that of $(VE)_2$. Additionally, we observed a decrease in pitch when increasing the pH from 7 to 8, which again suggested a correlation between the twist of a nanostructure and its lateral growth. We postulate that the linear charge density increases as a result of increasing the pH,[19] which likely increases the degree of twist of the ribbons. SAXS corroborated these cryo-TEM results by showing a decrease in slope, from −2 for pH 8 to −1.7 for pH 9 in the low-q regime (Figure S8). This decrease in slope can be attributed to a switch from large lamellar structures, like the nanobelt, to morphologies with more finite widths.

We then determined if increasing electrostatic repulsion had the same effect on β-sheet twisting as increasing the number of (VE) residues. Interestingly, a red-shift was no longer observed as pH was increased from pH 7 to pH 8 (Figure 4E). The absence of a red shift at pH 8 suggests that the twist of the β-sheet was not changing upon increased levels of deprotonation, even though changes were observed in nanostructure dimensions by cryo-TEM. Moreover, a slight blue-shift was observed at pH 9 compared to the CD spectrum at lower pH, which contained the thinnest nanostructures of the three (Figure 4C). This blue-shift at the highest pH studied suggests a change in molecular packing; previous reports have attributed a blue-shift of the minimum ellipticity to the disruption of hydrogen bonding of oligopeptides.[45] Additionally, the more pronounced maximum at 200 nm for pH 9 is comparable to computational studies of CD spectra for twisted amyloid peptides.[44] We interpret the differences in CD patterns with changes in pH as an indication that decreases in nanostructure widths in this case are directly linked to electrostatic repulsion.

Conclusions

A systematic study has been carried out to identify molecular structure factors controlling lateral dimensions and morphology of one-dimensional assemblies of peptide amphiphiles with β-sheet secondary structure. We showed that these flat β-sheet assemblies tend to twist as the length of the peptide sequence increases, leading to the suppression of lateral growth and eventual transformation to cylindrical morphology. Results obtained here demonstrate that peptide amphiphile sequences can profoundly affect their supramolecular morphologies in water and thus potentially affect their well known bioactivity.

Supplementary Material

Refer to Web version on PubMed Central for supplementary material.

Acknowledgments

This work was supported by the National Science Foundation (NSF Grant No. DMR0605427). TJM is supported by a NCI Center for Cancer Nanotechnology Excellence grant 1U54CA119341; and a Graduate Research Fellowship from the National Science Foundation. Transmission electron microscopy images were taken in the Biological Imaging Facility at Northwestern University. Circular Dichroism experiments were performed in the Keck Biophysics Facility at Northwestern University. SAXS experiments were performed at the DuPont-Northwestern-Dow Collaborative Access Team (DND-CAT) located at Sector 5 of the Advanced Photon Source (APS). DND-CAT is supported by E.I. DuPont de Nemours & Co., The Dow Chemical Company and Northwestern University. Use of the APS, an Office of Science User Facility operated for the U.S. Department of Energy (DOE) Office of

Science by Argonne National Laboratory, was supported by the U.S. DOE under Contract No. DE-AC02-06CH11357. We appreciate the help of Steven Weigand with SAXS. We thank Dr. John Matson and Dr. Liam Palmer for helpful discussions.

References

1. Aida T, Meijer EW, Stupp SI. Science. 2012; 335:813–817. [PubMed: 22344437]
2. De Greef TFA, Smulders MMJ, Wolffs M, Schenning APHJ, Sijbesma RP, Meijer EW. Chem. Rev. 2009; 109:5687–5754. [PubMed: 19769364]
3. Palmer LC, Stupp SI. Acc. Chem. Res. 2008; 41:1674–1684. [PubMed: 18754628]
4. Safinya CR, Raviv U, Needleman DJ, Zidovska A, Choi MC, Ojeda-Lopez MA, Ewert KK, Li Y, Miller HP, Quispe J, Carragher B, Potter CS, Kim MW, Feinstein SC, Wilson L. Adv. Mater. 2011; 23:2260–2270. [PubMed: 21506171]
5. Knowles TPJ, Buehler MJ. Nature Publishing Group. 2011:1–11.
6. Ryu J-H, Lee E, Lim Y-B, Lee M. J. Am. Chem. Soc. 2007; 129:4808–4814. [PubMed: 17381095]
7. Trent A, Marullo R, Lin B, Black M, Tirrell M. Soft Matter. 2011; 7:9572.
8. Mateos-Timoneda MA, Crego-Calama M, Reinhoudt DN. Chem. Soc. Rev. 2004; 33:363. [PubMed: 15280969]
9. Palmans ARA, Meijer EW. Angew. Chem. Int. Ed. 2007; 46:8948–8968.
10. Selinger JV, Spector MS, Schnur JM. J. Phys. Chem. B. 2001; 105:7157–7169.
11. Sawa Y, Ye F, Urayama K, Takigawa T, Gimenez-Pinto V, Selinger RLB, Selinger JV. Proceedings of the National Academy of Sciences. 2011; 108:6364.
12. Smith DK. Chem. Soc. Rev. 2009; 38:684. [PubMed: 19322462]
13. Matsumura Y, Maeda H. Cancer Research. 1986; 46:6387. [PubMed: 2946403]
14. Gratton SEA, Ropp PA, Pohlhaus PD, Luft JC, Madden VJ, Napier ME, DeSimone JM. Proceedings of the National Academy of Sciences. 2008; 105:11613.
15. Geng Y, Dalhaimer P, Cai S, Tsai R, Tewari M, Minko T, Discher DE. Nature Nanotechnology. 2007; 2:249–255.
16. Weisel JW, Nagaswami C, Makowski L. Proceedings of the National Academy of Sciences. 1987; 84:8991.
17. Lara C, Adamcik J, Jordens S, Mezzenga R. Biomacromolecules. 2011; 12:1868–1875. [PubMed: 21466236]
18. Adamcik J, Jung J-M, Flakowski J, De Los Rios P, Dietler G, Mezzenga R. Nature Nanotechnology. 2010; 5:423–428.
19. Adamcik J, Mezzenga R. Soft Matter. 2011; 7:5437.
20. Dietz H, Douglas SM, Shih WM. Science. 2009; 325:725–730. [PubMed: 19661424]
21. Ziserman L, Mor A, Harries D, Danino D. Phys. Rev. Lett. 2011; 106:238105. [PubMed: 21770548]
22. Yang Y, Meyer R, Hagan M. Phys. Rev. Lett. 2010; 104
23. Fishwick CWG, Beevers AJ, Carrick LM, Whitehouse CD, Aggeli A, Boden N. Nano Lett. 2003; 3:1475–1479.
24. Aggeli A, Nyrkova I, Bell M, Harding R, Carrick L, McLeish T, Semenov A, Boden N. Proceedings of the National Academy of Sciences. 2001; 98:11857.
25. Goldsbury CS, Wirtz S, Müler SA, Sunderji S, Wicki P, Aebi U, Frey P. Journal of Structural Biology. 2000; 130:217–231. [PubMed: 10940227]
26. Manning MC, Illangasekare M, W Woody R. Biophysical Chemistry. 1988; 31:77–86. [PubMed: 3233294]
27. Adamcik J, Castelletto V, Bolisetty S, Hamley IW, Mezzenga R. Angew. Chem. Int. Ed. 2011; 50:5495–5498.
28. Hartgerink JD, Beniash E, Stupp SI. Science. 2001; 294:1684–1688. [PubMed: 11721046]
29. Hartgerink JD, Beniash E, Stupp SI. Proceedings of the National Academy of Sciences. 2002; 99:5133.

30. Cui H, Webber MJ, Stupp SI. Biopolymers. 2010; 94:1–18. [PubMed: 20091874]
31. Webber MJ, Tongers J, Newcomb CJ, Marquardt KT, Bauersachs J, Losordo DW, Stupp SI. Proceedings of the National Academy of Sciences. 2011; 108:13438–13443.
32. Mata A, Geng Y, Henrikson KJ, Aparicio C, Stock SR, Satcher RL, Stupp SI. Biomaterials. 2010; 31:6004–6012. [PubMed: 20472286]
33. Tysseling-Mattiace VM, Sahni V, Niece KL, Birch D, Czeisler C, Fehlings MG, Stupp SI, Kessler JA. Journal of Neuroscience. 2008; 28:3814–3823. [PubMed: 18385339]
34. Soukasene S, Toft DJ, Moyer TJ, Lu H, Lee H-K, Standley SM, Cryns VL, Stupp SI. ACS Nano. 2011; 5:9113–9121. [PubMed: 22044255]
35. Toft DJ, Moyer TJ, Standley SM, Ruff Y, Ugolkov A, Stupp SI, Cryns VL. ACS Nano. 2012:120828094420001.
36. Jiang H, Guler MO, Stupp SI. Soft Matter. 2007; 3:454.
37. Pashuck ET, Cui H, Stupp SI. J. Am. Chem. Soc. 2010; 132:6041–6046. [PubMed: 20377229]
38. Cui H, Muraoka T, Cheetham AG, Stupp SI. Nano Lett. 2009; 9:945–951. [PubMed: 19193022]
39. Castelletto V, Hamley IW, Perez J, Abezgauz L, Danino D. Chem. Commun. 2010; 46:9185.
40. Pashuck ET, Stupp SI. J. Am. Chem. Soc. 2010; 132:8819–8821. [PubMed: 20552966]
41. Kline SR. J Appl Crystallogr. 2006; 39:895–900.
42. Guilbaud J-B, Saiani A. Chem. Soc. Rev. 2011; 40:1200. [PubMed: 21113529]
43. Pashuck ET, Cui H, Stupp SI. J. Am. Chem. Soc. 2010; 132:6041–6046. [PubMed: 20377229]
44. Hamley IW, Nutt DR, Brown GD, Miravet JF, Escuder B, Rodríuez-Llansola F. J. Phys. Chem. B. 2010; 114:940–951. [PubMed: 20039666]
45. Capes JS, Kiley PJ, Windle AH. Langmuir. 2010; 26:5637–5644. [PubMed: 20334410]

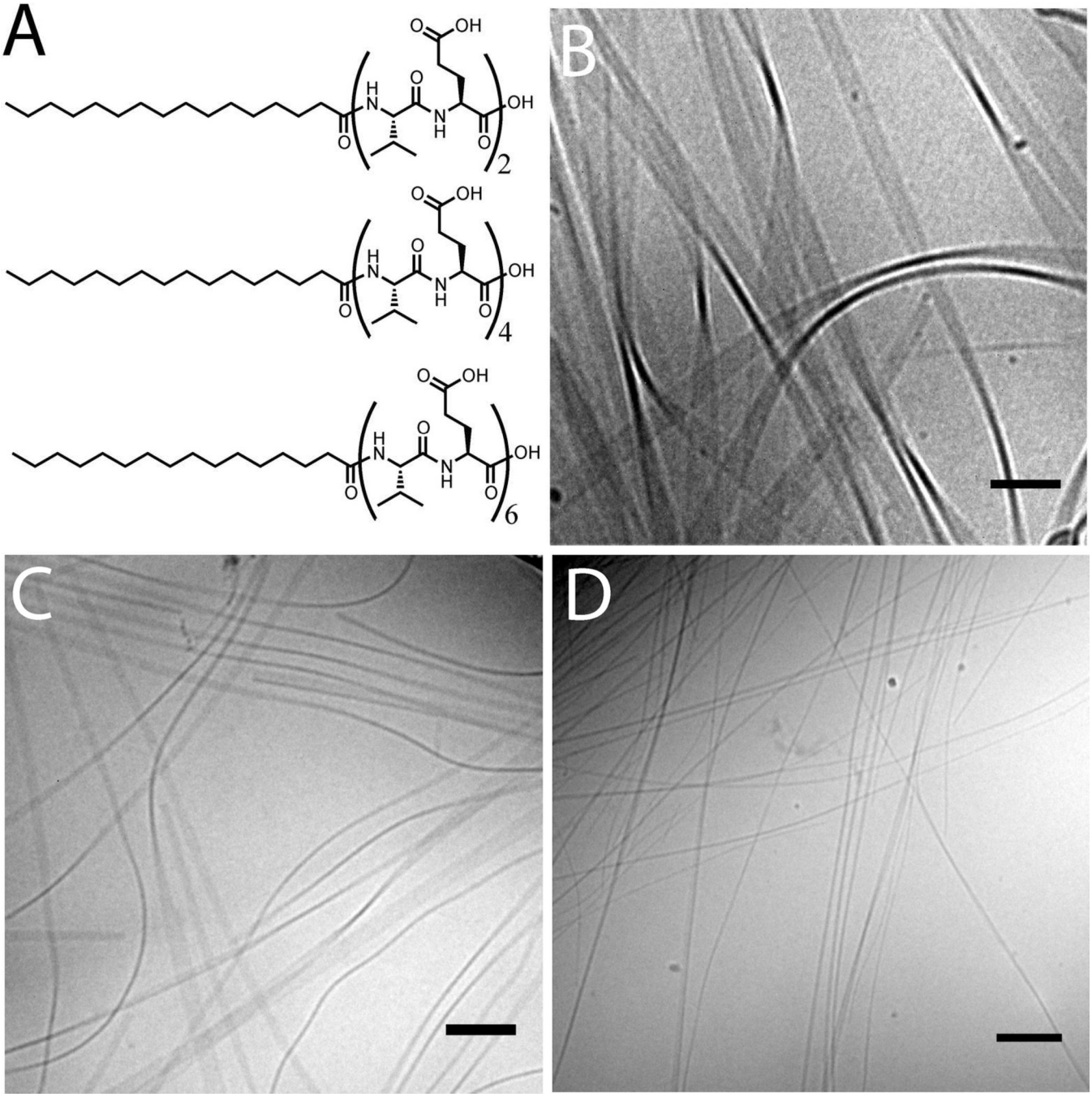

Figure 1.
(A) Chemical structures of $(VE)_2$, $(VE)_4$, and $(VE)_6$. (B–D) Cryogenic transmission electron micrographs of $(VE)_2$, $(VE)_4$, and $(VE)_6$ nanostructures formed in 5 mM solutions of PA. Scalebars: 200 nm.

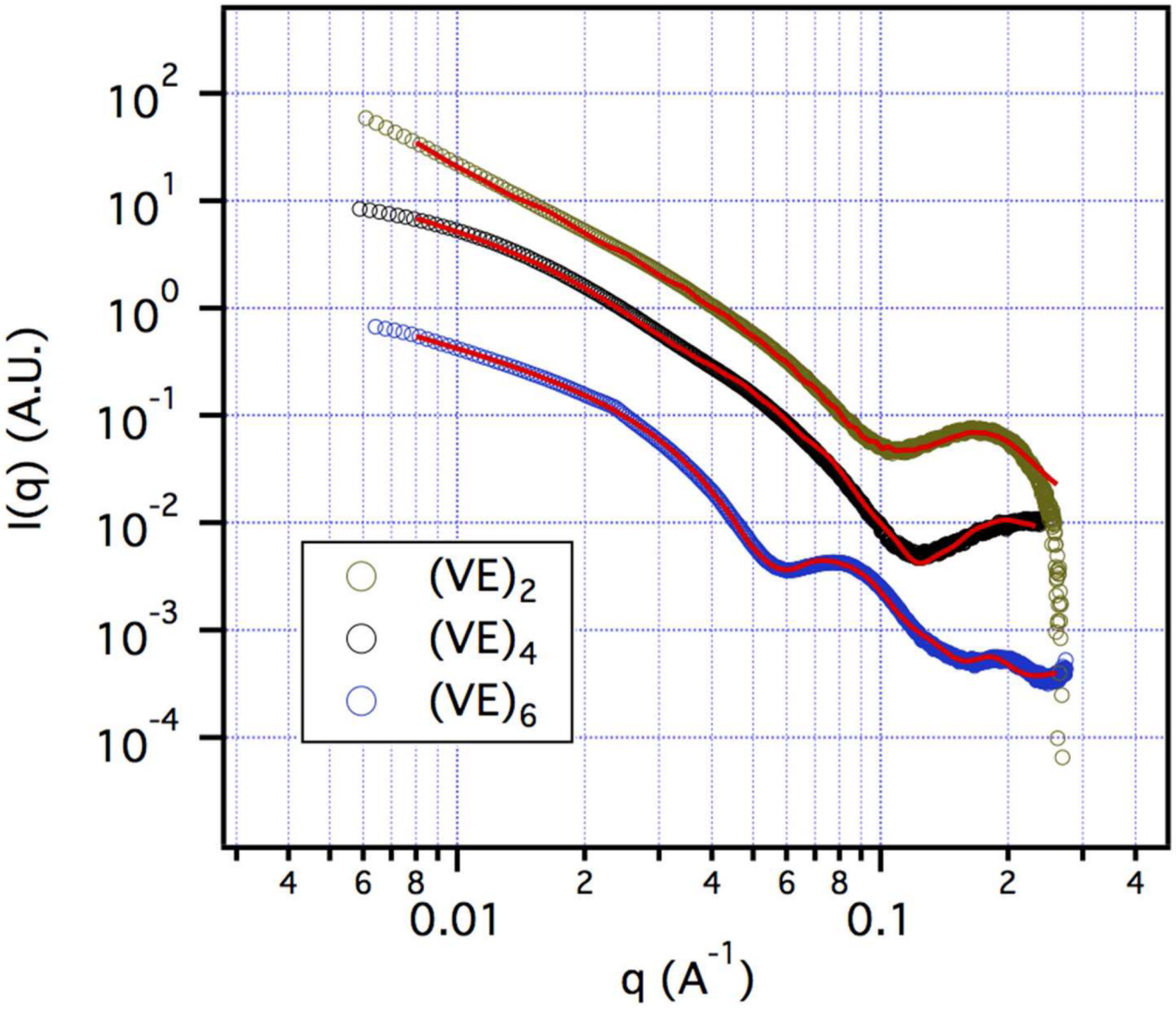

Figure 2.
Scattering profiles of 5mM solutions of $(VE)_2$, $(VE)_4$, and $(VE)_6$ fitted with core-shell parallelepiped fits (solid red lines). Scattering intensities were adjusted for clarity.

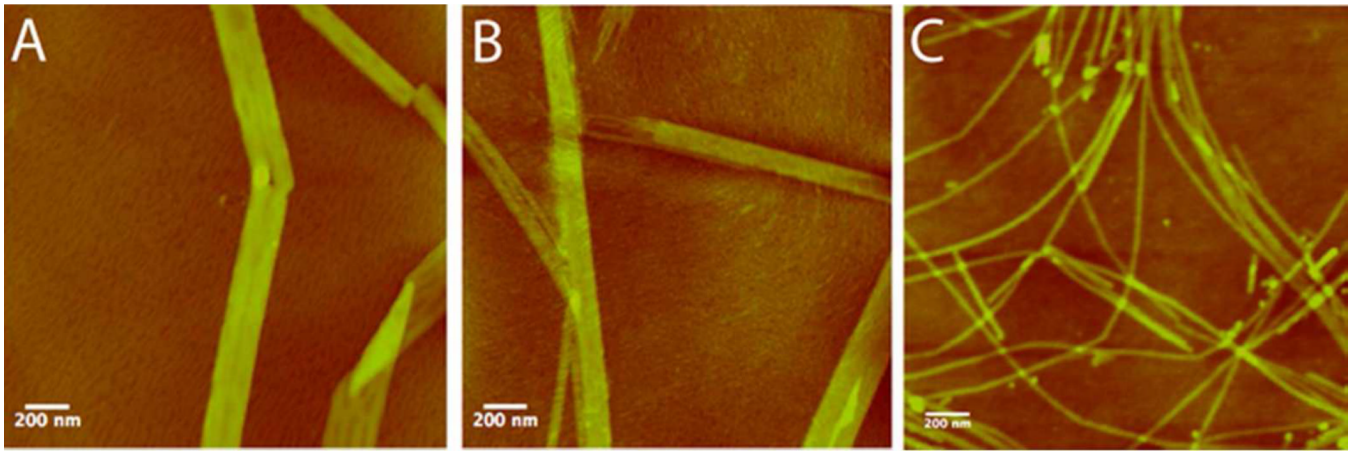

Figure 3.
(A–C) Atomic force microscopy images of dried films of 1 mM solutions of $(VE)_2$, $(VE)_4$, and $(VE)_6$.

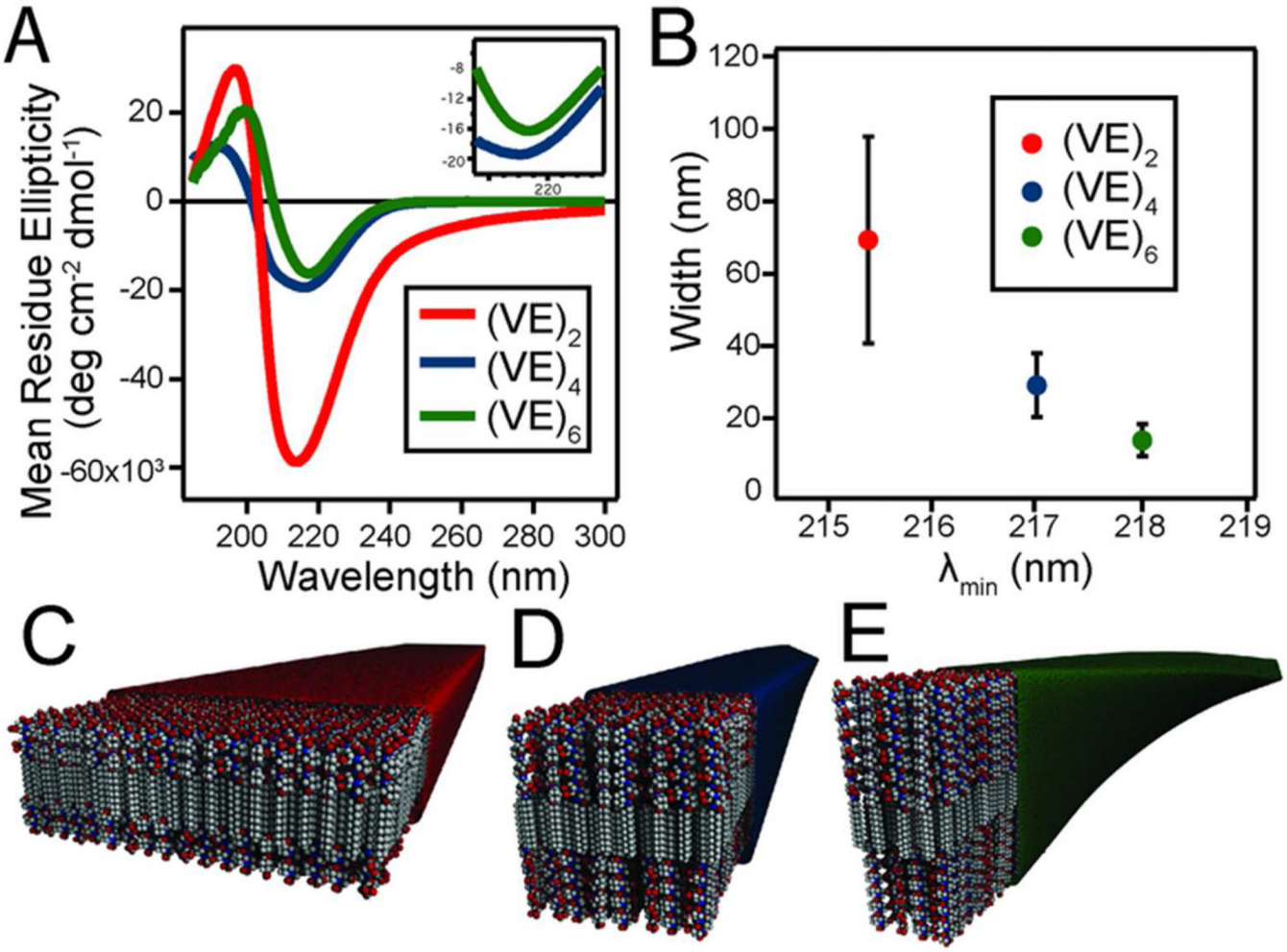

Figure 4.

(A) Circular dichroism of $(VE)_2$, $(VE)_4$, and $(VE)_6$ PAs. Inset shows the shift in minima for $(VE)_4$ and $(VE)_6$. (B) Red-shifting of PAs appears correlated with nanostructure width, as measured from cryo-TEM images. (C–E) Schematics of the proposed structures for $(VE)_2$, $(VE)_4$, and $(VE)_6$.

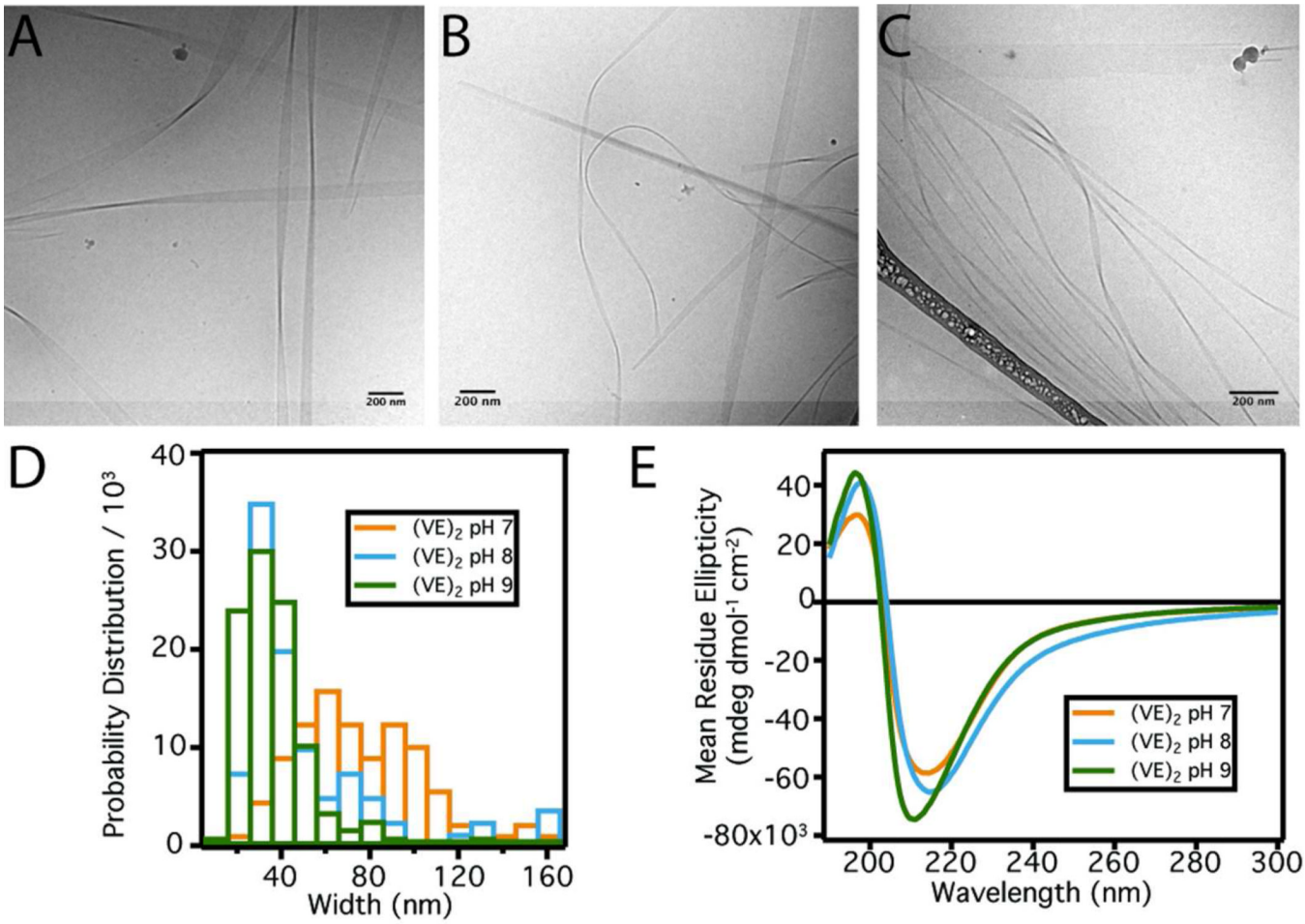

Figure 5.

(A–C) Cryogenic transmission electron micrographs of 5 mM solutions of $(VE)_2$ PA at pH 7, 8, and 9. (D) Width distributions of $(VE)_2$ PA at varying pH, as measured by cryo-TEM images. (E) Circular dichroism of $(VE)_2$ PA at pH 7, 8, and 9.